A subspace-based resolution-enhancing image reconstruction method for few-view differential phase-contrast tomography

Huifeng Guan[a], **Charlotte K. Hagen**[b], **Alessandro Olivo**[b], **Mark A. Anastasio**[a*]
[a]Department of Biomedical Engineering, Washington University in St. Louis, St. Louis, MO, USA, 63130
[b]Department of Medical Physics and Biomedical Engineering, University College London, London, UK

Abstract. It is well-known that properly designed image reconstruction methods can facilitate reductions in imaging doses and data-acquisition times in tomographic imaging. The ability to do so is particularly important for emerging modalities such as differential X-ray phase-contrast tomography (D-XPCT),[1] which are currently limited by these factors. An important application of D-XPCT is high-resolution imaging of biomedical samples. However, reconstructing high-resolution images from few-view tomographic measurements remains a challenging task due to the high-frequency information loss caused by data incompleteness. In this work, a subspace-based (SuB) reconstruction strategy is proposed and investigated for use in few-view D-XPCT image reconstruction. By adopting a two-step approach, the proposed method can simultaneously recover high-frequency details within a certain region of interest (ROI) while suppressing noise and/or artifacts globally. The proposed method is investigated by use of few-view experimental data acquired by edge-illumination D-XPCT scanner.

Keywords: Differential X-ray phase-contrast tomography, few-view image reconstruction.

*Mark A. Anastasio, anastasio@wustl.edu

1 Introduction

X-ray phase-contrast imaging (XPCI) methods continue to be actively developed and investigated for characterizing soft tissue or biological samples that present limited X-ray absorption contrast.[2–8] A variety of XPCI methods have been proposed, which include propagation-based imaging,[9,10] crystal analyzer-based imaging,[11–13] grating-based imaging based on the Talbot or Talbot-Lau effect[3,14,15] and edge-illumination imaging.[16–19] Conventional implementations of the crystal analyzer-, grating-, and edge-illumination-based methods are generally referred to as differential XPCI methods, since they typically yield estimates of the one-dimensional (1D) derivative of the projected real-valued component of the refractive index distribution of an object. In this work, a tomographic implementation of differential XPCI is considered, referred to as differential X-ray phase-contrast tomography (D-XPCT). The goal of D-XPCT is to produce an estimate of

the real-valued component of the refractive index distribution, which describes the spatially variant refractive properties of an object.

It will be assumed that the tomographic data function, from which an estimate of the refractive index distribution is reconstructed, corresponds to 1D derivative with respect to the detector row coordinate of the two-dimensional (2D) Radon transform of the refractive index distribution. This tomographic data function can be established by application of a phase-retrieval method[3, 12, 20–22] to the measured intensity data. When the data function is know at a sufficiently large number of tomographic views,[23] image reconstruction in D-XPCT can be readily accomplished by use of a modified filtered backprojection (FBP) algorithm.[1, 24, 25]

However, in current implementations of D-XPCT, it may not be desirable to acquire data at a large number of tomographic view angles. This is because D-XPCT methods are currently limited by relatively long data-acquisition times and radiation exposures, which has hindered the widespread application of the method to *in vivo* applications. Since current implementations typically utilize a 'step-and-shoot' data-acquisition protocol, as opposed to the continuously rotating X-ray source and detector pair utilized in a clinical CT scanner, one way to mitigate this problem is to acquire tomographic measurements at a reduced number of view angles. The associated image reconstruction problem is generally referred to as a 'few-view' image reconstruction problem.[26, 27] It might be worth mentioning that recently a phase CT has been developed with a lab source using continuous rotation in a few minutes, but the limitation in that case is the approximation in the phase retrieval.

There exists a vast literature related to few-view image reconstruction.[26, 28–31] Modern few-view image reconstruction methods are optimization-based and typically utilize an iterative method to find a finite-dimensional estimate of the object function that approximately minimizes an objective

function subject to constraints. In the case of D-XPCT, the object function corresponds to the refractive index distribution. While existing few-view reconstruction methods can be adapted for use in D-XPCT,[32–35] there remains a need for improved methods for reconstructing high-resolution D-XPCT images from few-view measurements. Because few-view image reconstruction corresponds to an ill-conditioned inverse problem, a regularized solution must be computed; however the design of an effective regularization strategy is influenced by many factors, including the characteristics of the refractive index distribution to be estimated.

Regularization methods that promote object sparsity[26,36] are ubiquitous in the modern image reconstruction literature. Although total variation (TV) regularization has been employed widely, its effectiveness is degraded when the object's gradient map is not sparse.[32,37] To mitigate this problem, object sparsity can be promoted in a different transform domain in which the object is sparsely represented.[38] Analytical sparsifying transforms such as wavelets, curvelets, and finite differences can be employed. Alternatively, the sparsifying transform can be adaptively learned from a set of training data.[39,40] Moreover, multiple penalty functions can be employed in the objective function in order to obtain a balanced regularization,[41] or more complicated strategies can be employed that achieve local TV regularization effects in the image domain.[42] However, it remains challenging to design a regularization strategy that faithfully preserves fine object features in the reconstructed image when only few-view tomographic data are utilized.

In this work, a new method for few-view image reconstruction in D-XPCT is proposed and investigated. A distinctive feature of the method is that the sought-after object function is decomposed into two components that reside in distinct subspaces. One component corresponds to the high frequency components of the object function that reside within a certain region of interest (ROI). The radius of the ROI is determined by the spatial frequency content of the object function

and the number of tomographic view considered. This object component can be stably recovered from the few-view measurement data using a Penalized Least-Squares (PLS) estimator. The second component corresponds to the lower frequency components of the object function, over the entire support of the object. This object component, which is slowly varying, can be accurately estimated by use of a TV-regularized PLS estimator (PLS-TV). In this way, the high frequency components of the object function within the ROI can be faithfully preserved, while outside of the ROI lower-frequency components of the object can be accurately recovered and streak artifacts can be suppressed. The proposed subspace-based method is applied to few-view experimental data acquired by use of a benchtop edge-illuminiation D-XPCT system and its performance is compared to the conventional FBP and PLS-TV methods.

2 Background

2.1 D-XPCT imaging model in semi-discrete form

It will be assumed that all functions below are compactly supported and belong to weighted $\mathbb{L}^2$-spaces. For a function $f(\mathbf{r})$ that is compactly supported on a disk $D \subset \mathbb{R}^2$, the two-dimensional (2D) Radon transform of the function is defined as

$$(\mathcal{R}_c f)(s,\phi) = \int_{-r}^{r} f(\mathbf{r})\delta(s - \mathbf{r}\cdot\mathbf{n})d\mathbf{r}, \tag{1}$$

where $s \in (-r, r)$ denotes the detector row coordinate, $\phi \in (0, \pi)$ denotes the tomographic view angle, and $\mathbf{n} = \{\cos\phi, \sin\phi\}$ is a unit vector making angle ϕ to the x-axis.

Considering the case of few-view measurement data where only a finite number of views are available, the corresponding finite-view Radon transform can be defined by discretizing $\mathcal{R}_c$ with

respect to the tomographic view angle:

$$(\mathcal{R}f)(s,\phi_i) = \int_{-r}^{r} f(\mathbf{r})\delta(s-\mathbf{r}\cdot\mathbf{n_i})d\mathbf{r}, \tag{2}$$

where $\mathbf{n_i} = \{\cos\phi_i, \sin\phi_i\}$ and ϕ_i belongs to a set S that contains discrete tomographic view angles indexed with $i = 1, 2, ..., M$. Therefore, $\mathcal{R}$ is a compact operator from $\mathbb{L}_2(D)$ into $\mathbb{L}_2(Z)$, where $Z = [-r, r] \times S$.

The D-XPCT imaging model can be described as a finite-view differential Radon transform $\mathcal{H} = \mathcal{D}\mathcal{R}$, where $\mathcal{D}$ is a one-dimensional first-order derivative operator:

$$g(s,\phi_i) = \mathcal{H}f(\mathbf{r}) \equiv \mathcal{D}\mathcal{R}f(\mathbf{r}) = \frac{\partial}{\partial s}\int_{-r}^{r} f(\mathbf{r})\delta(s-\mathbf{r}\cdot\mathbf{n_i})d\mathbf{r}. \tag{3}$$

Here, $g(s,\phi_i)$ is a tomographic data function that is established by use of a phase retrieval method.[43–46]

The image reconstruction task in D-XPCT is to determine an estimate of $f(\mathbf{r})$, which represents the refractive index distribution, from knowledge of $g(s,\phi_i)$. When the data function $g(s,\phi_i)$ is determined at a large number of view angles, this can be accomplished by use of analytical image reconstruction algorithms.[47] For example, images can be reconstructed by use of a modifed FBP method as[1]

$$\hat{f}_{\text{FBP}} = \mathcal{R}^{\dagger}C_h g, \tag{4}$$

where † indicates the adjoint operator, and C_h is a filter kernel acting as the Hilbert transform scaled by a factor. Typically the scaling factor equals the angular spacing $\Delta\phi$ if all the projections are uniformly acquired over the π span. Here $\mathcal{R}^{\dagger}$, usually referred to as the back projection operator,

is mathematically equivalent to discretizing $\mathcal{R}_c^\dagger$ with respect to the variable ϕ:

$$(\mathcal{R}^\dagger g)(\mathbf{r}) = \sum_{i=1}^{M} [\int_{-r}^{r} g(s, \phi_i)\delta(s - \mathbf{r} \cdot \mathbf{n_i})ds]. \tag{5}$$

Note that Eq. (4) appears similar to the classical FBP algorithm for CT image reconstruction, where the reconstruction kernel has been modified. However, in the case of noisy and/or few-view measurement data, analytic reconstruction methods are known to be suboptimal and the use of iterative methods is highly desirable.

2.2 Null-space properties of finite-view Radon transform

The finite-view Radon transform $\mathcal{R}$ is a semi-discrete version of the classical Radon transform in which only discretization of the angular variable is performed. A unique and exact reconstruction of an arbitrary function is mathematically impossible when the tomographic data contains only a finite number of views. This implies that the finite-view Radon transform has a non-trivial null space. The functions in this null space, denoted as f_{null}, are invisible along the considered projection directions, or mathematically speaking, $\mathcal{R}f_{null} = \mathbf{0}$, where $\mathbf{0}$ is an infinite-dimensional zero vector defined in the range of $\mathcal{R}$. Correspondingly, the orthogonal complement of the null space is defined as measurable space.

By use of various mathematical tools, for example the orthogonal function series expansions or singular value decomposition, important insights into the null-space properties of the finite-view Radon transform have been established.[23,48–52] Defining a compact disc support of radius r, and assuming a set of M equispaced projections over π span, Logan[48] revealed that the 2D Fourier transform of any null-space function corresponding to the imaging operator $\mathcal{R}$ is negligible inside

a disc of radius Ω in Fourier space when

$$\Omega = M/(2\pi r), \tag{6}$$

as illustrated in figure 1(a), where the estimate holds when $M \gg \pi/2$.

As a direct consequence, a function whose 2D Fourier transform is concentrated within this frequency disk Ω can be reliably reconstructed from its M projections.[52] An intuitive illustration is provided in figure 1(b). If the frequency contents of the object do not fall into the null space of the finite-view Radon transform, the object can be accurately reconstructed. More rigorous mathematical proofs can be found in previous works.[23,50]

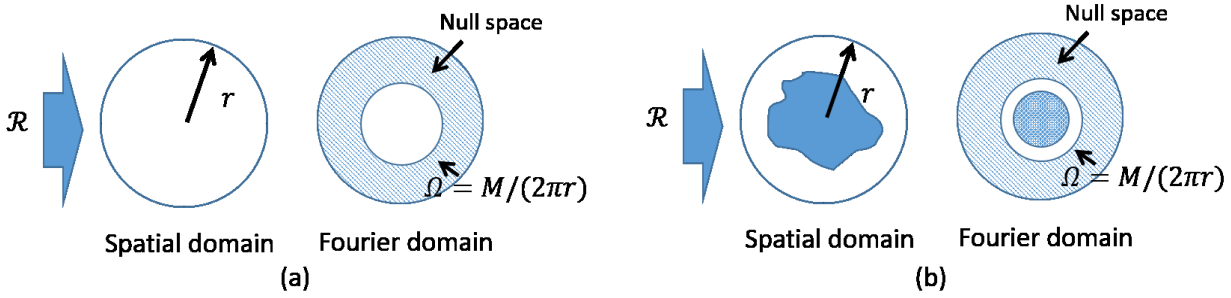

Fig 1 (a) The null-space functions of the finite-view Radon transform are contained exclusively outside a disk Ω in the Fourier domain, shown as the gray region. (b) If a to-be-imaged object has all the frequency contents confined to Ω without overlapping the null-space region, it means the object could be reliably reconstructed.

Remark 1: The above argument has been a long-time guide for determining the angular sampling requirements for a CT scan.[52] For non-trucated projections, the D-XPCT data set can be readily converted to a CT data set by use of an integral operator, without any information loss. So the conclusion is also valid for the D-XPCT imaging scenario.

Remark 2: For an imaging operator $\mathcal{R}$ with the support radius and number of views already defined, the above argument tells under what conditions the image can be reliably reconstructed,

which does not rely on any specific reconstruction algorithm. In practice, FBP-type algorithms taking the form of Eq. (4) have been widely implemented in CT, proving reliable reconstructions as long as the relationship of Eq. (6) is satisfied.[23,52,53]

Remark 3: A compactly supported object theoretically does not have a strictly band-limited frequency distribution; therefore one should keep in mind that the argument only holds when we can assume the measurements are quasi-band-limited, which is the case in many practical implementations.[54]

3 Motivation for subspace-based image reconstruction

3.1 Revisiting the FBP algorithm

When the imaging system corresponds to a field of view (FOV) of radius r that does not meet the requirement in Eq. (6), the aforesaid angular sampling is insufficient for an accurate reconstruction when the FBP algorithm is employed. From the perspective of the Fourier slice theorem, the acquired data suffer a significant high-frequency information loss, and a blurred reconstructed image is expected. However, it is interesting that, though the conventional FBP algorithm is known to give rise to streak-like aliasing artifacts, the reconstructed image looks sharper and more resolution-enhanced in comparison to the image that reflects the measurable component of the object.[55] Here, the measurable component f_{meas} is defined as the part of the object that lies in the measurable space of the operator $\mathcal{R}$. It can be interpreted as the least-square estimate of the object that has the minimum L2-norm, known as the pseudo-inverse solution, which can be computed by use of the Landweber iterative algorithm or other inversion methods.[56]

In order to better interpret an image produced by use of the FBP algorithm, the to-be-imaged object f can be decomposed into two components as $f = Wf + (1 - W)f$. Here, W is a 0-1

function that performs as a circular mask with the center at the origin, such that

$$W(\vec{\mathbf{r}}) = \begin{cases} 1 & \text{if } \|\vec{\mathbf{r}}\| < r' \\ 0 & \text{elsewhere,} \end{cases} \tag{7}$$

where the radius r' is determined as

$$r' = M/(2\pi\Omega). \tag{8}$$

As introduced in Eq. (6), Ω denotes the maximum spatial frequency of the object. Motivated by the previous null-space properties of the finite-view Radon transform, W specifies the largest ROI that can potentially be reliably reconstructed, as will be discussed below.

Denote the FBP reconstruction operator as $\mathcal{B} = \mathcal{R}^{\dagger} C_h$ for a given finite-view D-XPCT problem, where the back projection operator $\mathcal{R}^{\dagger}$ and filter C_h are defined as in Eq. (4). Assuming consistent data $g = \mathcal{H}f$, an image reconstructed by use of the FBP algorithm can be expressed as

$$\hat{f}_{\text{FBP}} = \mathcal{B}g = W\mathcal{B}g + (1 - W)\mathcal{B}g. \tag{9}$$

The reconstructed image within a designated ROI of radius r' can be isolated by applying the mask W on $\hat{f}_{\text{FBP}}$

$$\begin{aligned} W\hat{f}_{\text{FBP}} =& W\mathcal{B}g \\ =& W\mathcal{B}\mathcal{H}f \\ =& W\mathcal{B}\mathcal{H}Wf + W\mathcal{B}\mathcal{H}(1 - W)f. \end{aligned} \tag{10}$$

The first term in Eq. (10), $W\mathcal{B}\mathcal{H}Wf$, describes an image of the ROI reconstructed by use of the measurements that are solely produced from the structures inside the same ROI, as illustrated

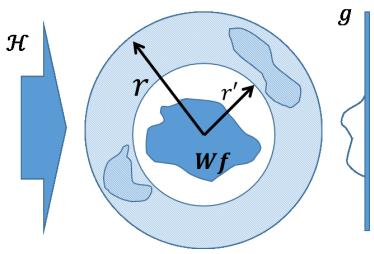

Fig 2 The illustration of the reconstruction over the support r and with a virtual mask W. FBP algorithm ensures that the reconstruction of ROI within r' is not affected by the masked region.

by the projection profile shown in Figure 2. Note that $\mathcal{B}\mathcal{H}Wf$ is the reconstructed image defined in the whole support, in which the area outside the radius r' is not zero but may contain streak artifacts when the number of projection views is not sufficient. However, due to the properties of the back projection operator $\mathcal{R}^{\dagger}$, the FBP method ensures that the reconstruction of the ROI of radius r' is independent of that for the masked region. Therefore, reconstructing the designated ROI is equivalent to a conventional reconstruction problem that has a smaller FOV of radius r'. If $\Omega = M/(2\pi r')$ holds, it is reasonable to directly apply the argument stated in Section 2.2 to establish that this ROI can be reliably reconstructed by use of the FBP algorithm. Mathematically speaking, $W\mathcal{B}\mathcal{H}Wf = Wf$.

The second term of Eq. (10), $W\mathcal{B}\mathcal{H}(1-W)f$, namely represents the streak artifacts present in the ROI that is backprojected from the source $(1-W)f$ corresponding to the structures outside the ROI. It can be denoted as an error term ϵ, and will be further discussed it in Section 3.2.

In summary, by rewriting Eq. (10) it can be concluded that

$$W\hat{f}_{\text{FBP}} = Wf + \epsilon. \tag{11}$$

This suggests that, for few-view tomographic reconstruction, although the information is not sufficient enough to accurately recover the entire image by use of an un-regularized reconstruction

operator, there is still an opportunity to reliably estimate the object within a restricted ROI when ϵ is small.

3.2 The recovery of the object's high-frequency contents

Given the imaging operator $\mathcal{H}$ and the data function g, an optimization problem is proposed based on Eq. (11) in order to extract certain high-frequency components of f that are usually difficult to retrieve:

$$\begin{aligned} f_1 &= \underset{f}{\operatorname{argmin}} \|f\|^2 \\ s.t.\ &\mathcal{H}f = (C-1)g, \end{aligned} \tag{12}$$

where the filter $C = \mathcal{H}\mathcal{R}^{\dagger}C_h$, and C_h is a scaled Hilbert transform operator as specified in Eq. (4). Mathematically, one can demonstrate that

$$Wf_1 = Wf_{\text{null}} + \epsilon, \tag{13}$$

where the determination of W is guided by the aforesaid rule of Eq. (8), and f_{null} denotes the null component of the object in terms of the imaging operator $\mathcal{H}$. Details regarding this interpretation are provided in the appendix.

As suggested by the Fourier slice theorem, f_{null} mainly contains high-frequency information that is insufficiently sampled in the Fourier domain. As a consequence, Eq. (13) suggests that the recovery of Wf_1 can yield useful high-frequency information regarding the object within the ROI of radius r', which is generally a challenge for few-view image reconstruction methods.

Note that the solution of Eq. (12) also satisfies

$$f_1 = \underset{f}{\operatorname{argmin}} \|\mathcal{H}f - (C-1)g\|^2, \tag{14}$$

when a Landweber-type iterative algorithm is employed starting from a zero intial guess.[57]

Remark 1: Since W is non-invertible, it should be noted $\mathcal{H}W f_{null} = \mathbf{0}$ is generally not true. Therefore by definition $W f_{null}$ is not a null-space function of the imaging system, and the recovery of $W f_{null}$ does not violate linear operator theory.

Remark 2: Under certain conditions, the error term ϵ could be insignificant. This could occur, for example, if the outside-ROI structures are weak in magnitude or sparse in spatial distribution. Also, if the outside-ROI structures corresponds to lower frequencies, ϵ can be negligible. This could be understood by a similar analysis as stated in section 2.2, which implies a lower-frequency object could have a larger "artifact-free" zone. Particularly, if the outside-ROI structures have $\Omega \leqslant M/(2\pi R)$, then they won't produce any streak artifacts over the entire object support R, and ϵ is consequently zero.

4 Subspace-based image reconstruction method

4.1 General forms of the discrete imaging model

Many iterative image reconstruction algorithms require a discrete imaging model, and a natural way to obtain this is to discretize the semi-continuous model in Eq. (3). When a digital detector is employed, the data function corresponds to an ordered collection of numbers. Since the

reconstruction problem is inherently 2D, we will denote the discrete data function as

$$g[k, \phi_i] = g(s, \phi_i)|_{s=k\Delta_d}, \tag{15}$$

where k is integer-valued detector element index along the transverse direction, and Δ_d denotes the detector element dimension. Let the vector $\mathbf{g} \in \mathbb{R}^{K\times M}$ denote a lexicographically ordered representation of $g[k, \phi_i]$. The dimension of $\mathbf{g}$ is the product of the number of detector row elements K and the number of view angles M.

In order to obtain a finite-dimensional approximate representation of the object function, a linear N-dimensional approximation of $f(\mathbf{r})$ can be formed as

$$f_a(\mathbf{r}) = \sum_{n=0}^{N-1} \tilde{f}_n \beta_n(\mathbf{r}), \tag{16}$$

where the subscript a indicates that $f_a(\mathbf{r})$ is an approximation of $f(\mathbf{r})$, $\{\beta_n(\mathbf{r})\}$ are a set of expansion functions, and $\{\tilde{f}_n\}$ are the corresponding expansion coefficients. Let $\mathbf{f}$ be a $N \times 1$ vector of expansion coefficients that has an n-th element given by $\tilde{f}_n$. Rather than the conventional pixel basis functions, the Kaiser-Bessel window expansion functions[33,58] (or usually referred to as "blobs") were employed in this study. This choice has the attractive feature that the derivative of the Radon transforms of the expansion functions can be computed analytically, thereby circumventing the need to numerically approximate them.

With the defined discrete data function $\mathbf{g}$ and object function $\mathbf{f}$, a system matrix $\mathbf{H}$ employing the generalized Kaiser-Bessel window functions was constructed[32] and a discrete imaging model

was formed as

$$\mathbf{g} = \mathbf{H}\mathbf{f}. \tag{17}$$

It should be noted that some blob parameters (e.g. radius, specific shape) may also affect the system matrix stablity and the reconstruction performance. The optimal parameter selections have been described in the literature.[32,59,60] Equation (17) can be employed with iterative image reconstruction algorithms for estimation of $\mathbf{f}$ from knowledge of $\mathbf{g}$ and $\mathbf{H}$. From the estimated $\mathbf{f}$, the object function estimate - the sought after image - can be obtained by use of Eq. (16).

4.2 Proposed iterative reconstruction method

Equation (11) implies that, for a given object, the FBP algorithm can produce images that depict high-frequency structures within a ROI whose radius is dependent on the number of tomographic views. However, the FBP algorithm usually does not effectively mitigate noise. Also, it produces severe streak artifacts outside the ROI when the number of views is insufficient. Meanwhile, the conventional TV-regularized iterative algorithm can effectively suppress noises and artifacts, but it also brings the risk of removing desired subtle structures.

In order to synergically combine the two reconstruction methods, we propose a subspace-based (SuB) reconstruction strategy, and reconstruct the images in a two-step, iterative approach that can be more robust against the noise.

Similar to the decomposition step described in the previous section, the reconstructed image $\mathbf{f}$ is denoted as the sum of two images $\mathbf{f_1}$ and $\mathbf{f_2}$ by

$$\mathbf{f} = W\mathbf{f}_1 + \mathbf{f}_2, \tag{18}$$

where $\mathbf{f_1}$ and $\mathbf{f_2}$ can be computed respectively via a two-step approach as shown in Eq. (19) and (20). We first compute $\mathbf{f}_1$ by solving

$$\mathbf{f}_1 = \underset{\mathbf{f}}{\operatorname{argmin}} \|\mathbf{H}\mathbf{f} - (C-1)\mathbf{g}\|^2, \tag{19}$$

with a gradient-descent algorithm and a zero initial guess. Subsequently, the object component $W\mathbf{f}_1$ is fixed and $\mathbf{f}_2$ is estimated as:

$$\mathbf{f}_2 = \underset{\mathbf{f}}{\operatorname{argmin}} \|\mathbf{H}(W\mathbf{f}_1 + \mathbf{f}) - \mathbf{g}\|^2 + \lambda\|\mathbf{f}\|_{TV}, \tag{20}$$

where $\|\cdot\|_{TV}$ indicates the total-variation semi norm.[42]

As suggested in Section 3.2, the first sub-problem [Eq. (19)] produces an estimate of $W\mathbf{f}_1$ that mainly contains the high-frequency contents of the object inside the designated ROI. In the second sub-problem [Eq. (20)], a TV-penalized least square (PLS-TV) estimator is employed for estimating $\mathbf{f}_2$. Note that by subtracting the contribution of high-frequency component from the measurements, $\mathbf{f}_2$ will mainly contain low-frequency contents, which is considered smoother and therefore more suitable for the application of TV regularization.

Therefore, the proposed sub-space image reconstruction method, referred to as the Sub-PLS-TV method, includes the following potential benefits:

- The high-frequency details within the designated ROI can be stably recovered from measured few-view data.

- The global TV regularization is still employed for the purpose of suppressing noise and streak artifacts over the entire object domain.

- Since the two subspaces are naturally constrained in the second sub-problem, in the reconstructed image the transitions at the ROI boundaries are smooth.

Below, the proposed Sub-PLS-TV method, the FBP method, and the conventional PLS-TV method will be compared through numerical studies. The PLS-TV method corresponds to iteratively solving the following optimization problem

$$\hat{\mathbf{f}}_{\text{PLS}} = \underset{\mathbf{f}}{\operatorname{argmin}} \|\mathbf{Hf} - \mathbf{g}\|^{\mathbf{2}} + \lambda \|\mathbf{f}\|_{\mathbf{TV}}, \tag{21}$$

which has been widely used for few-view CT image reconstruction.[42] A modern iterative reconstruction algorithm based on the FISTA acceleration framework[61] is employed for the two iterative methods.

5 Results

5.1 Computer-simulation studies

Computer-simulation studies were conducted to demonstrate and validate the proposed SuB-PLS-TV image reconstruction method. A 1024×1024 numerical phantom was generated, shown in Fig. 3, which contained a lumpy background with slowly varying magnitude and a disk with fast varying ripple fluctuations. Differential phase-contrast measurement data corresponding to 90 tomographic views evenly distributed over 180 degrees were generated by projecting the phantom using the system matrix $\mathbf{H}$ introduced in Section 4.1. Consequently, the system matrix used for data generation exactly matches the one used for reconstruction in this simulation study. In order to mitigate the inverse crime, here 5% Gaussian noise was added in the simulated data. Note that

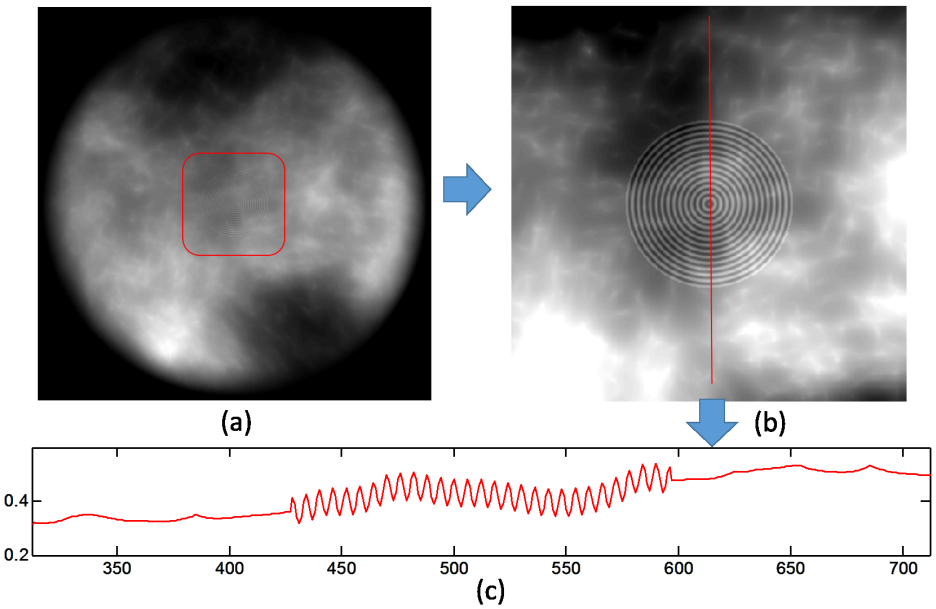

Fig 3 (a) The complete phantom. (b) A zoomed-in region of the central part of the phantom with adjusted gray-value window. The dashed circle indicates the designated ROI where the capability of reconstructing high-frequency structures is expected. (c) The extracted profile of the phantom across the center.

the model mismatch will be inherently present in the experimental study that is discussed in the next section.

In the phantom, the random background was generated based on the recommended parameters for mimicking the statistical texture of mammographic images.[62] The rippled disk represents the high-frequency details that normally bring challenges for few-view image reconstruction. For simplicity, the ripple was designed to have a constant spatial frequency at 6 pixels/cycle that was verified as the phantom's upper frequency limit by examing its 2D Fourier spectrum. Therefore, based on Eq. (6), a ROI could be designated with the radius $r = M/(2\pi\Omega) = 86$ pixels in which the high frequency structures are expected to be well recovered. In this study, the radius of the rippled disk was also made as large as r for the purpose of demonstrating the maximum ability of reconstructing high-frequency structures.

We compared the performances of three methods: FBP, PLS-TV, and the proposed SuB-PLS-

TV method. For both iterative methods, the regularization parameter λ was swept over a wide range to show the overall tendency of image quality. A series of typical reconstructed images corresponding to progressively increasing TV parameters (i.e. $1e^{-4}$, $1e^{-3}$, $1e^{-2}$ and $1e^{-1}$) are shown in Figs. 4 and 5, for the designated ROI region and an outside-ROI region, respectively.

In the designated ROI (Fig. 4), the conventional PLS-TV method was ineffective at recovering the high-frequency ripples of the disk, no matter how we tuned the regularization parameter. TV regularization smooths the noisy background but meanwhile suppresses high-frequency details. As opposed to this, the proposed SuB-PLS-TV method selectively applies the TV regularization to the low-frequency subspace, and is thus able to preserve the high-contrast ripples within the ROI. Also, the proposed method still gains the benefits of noise suppression by using TV regularization, which is a significant advantage over the analytical FBP method. Since the lumpy background contains mostly low-frequency contents, there are no discernible streak artifacts shown in the designated ROI, suggesting that the error term in Eq. (13) is negligible.

In an outside-ROI region (Fig. 5), where streak artifacts occur in the image reconstructed by the FBP method, the SuB-PLS-TV method still outperforms the alternative iterative method in terms of artifact suppression. This is credited to the novel cost function design of the sub-problem in Eq. (20). The subtraction of the contribution of $W\mathbf{f}_1$ from the measurement data leads to more accurate estimation of $\mathbf{f}_2$ representing the accurate low-frequency structures over the entire image.

Line profiles were extracted from the reconstructed images and superimposed on the corresponding profiles through the true phantom. The profile through the center, as depicted in Fig. 3, crosses the designated ROI and an outside-ROI region where the streak artifacts would occur. Figure 6 shows a series of profiles corresponding to the PLS-TV reconstructed images with increasing TV regularization parameters. Figure 7 shows a series of profiles corresponding to the SuB-PLS-

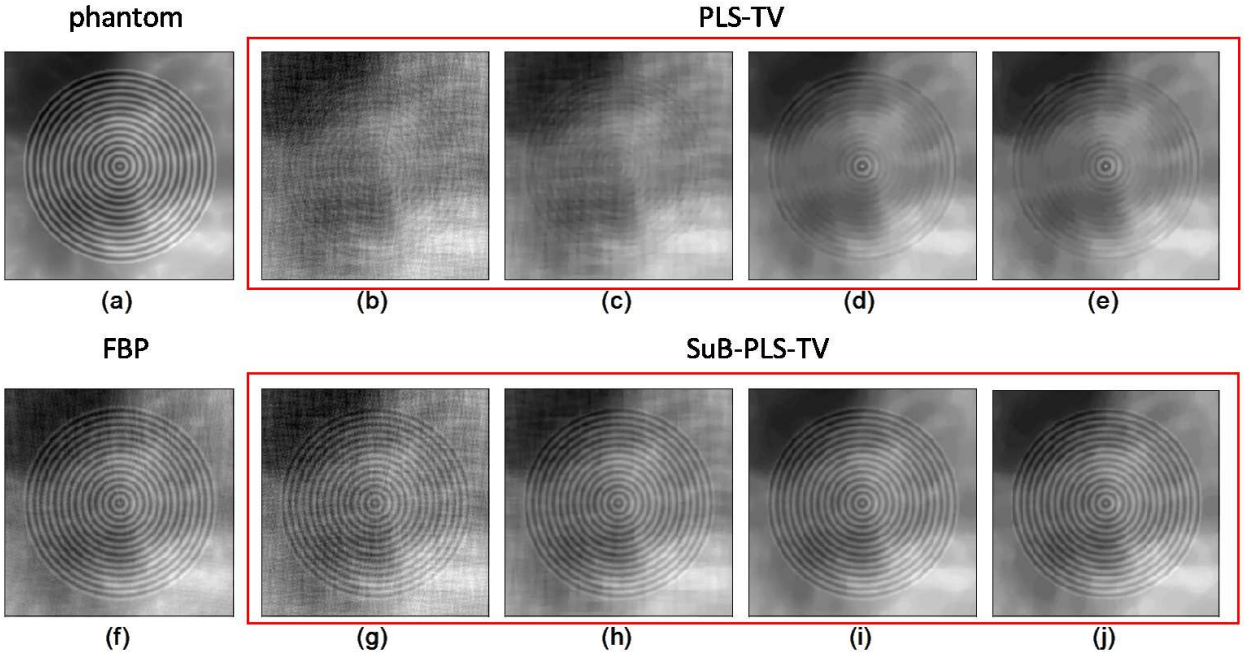

Fig 4 The comparison of reconstructed images inside the designated ROI. (a) Phantom; (b)-(e) The PLS-TV method with increasing TV regularization parameter values; (f) FBP method; (g)-(j) The proposed SuB-PLS-TV method with progressively increasing TV regularization parameter values.

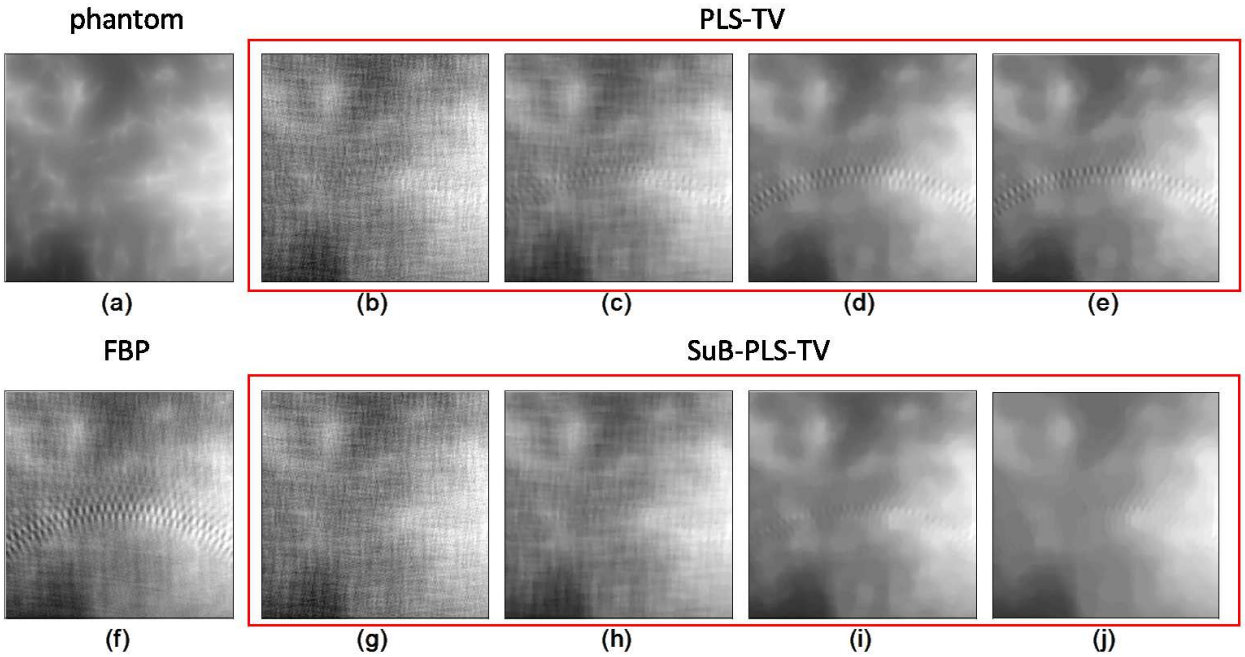

Fig 5 The comparison of reconstructed images outside the designated ROI. (a) Phantom; (b)-(e) The PLS-TV reconstruction results with increasing TV regularization parameter values; (f) FBP method; (g)-(j) The proposed SuB-PLS-TV reconstruction results with progressively increasing TV regularization parameter values.

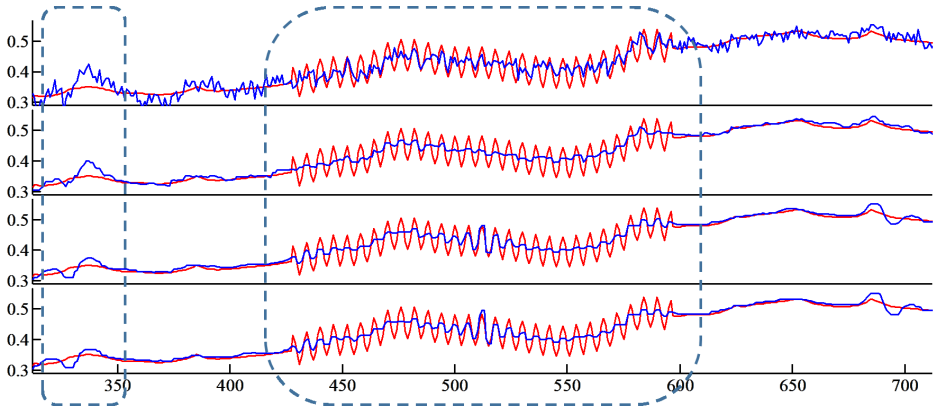

Fig 6 The profiles extracted from the conventional PLS-TV reconstructed images with increasing regularization parameter values (blue) and the corresponding ground truth (red).

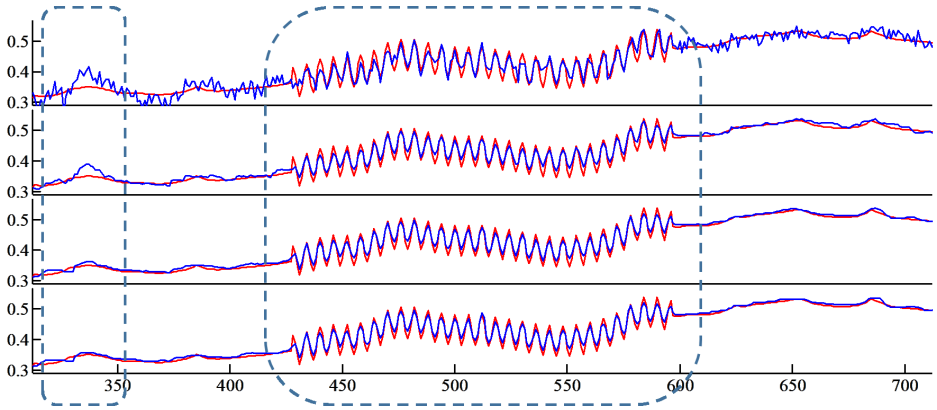

Fig 7 The profiles extracted from the SuB-PLS-TV reconstructed images with increasing regularization parameter values (blue) and the corresponding ground truth (red).

TV results with increasing TV regularization parameters. Profiles through the reconstructed images for the inside and outside ROI are highlighted by dashed squares. Again, the SuB-PLS-TV method yields a reconstruction result that is visually more consistent with the ground truth. By tuning the regularization parameter, it performs better than the conventional PLS-TV method in terms of balancing the recovery of high-frequency ripples and the suppression of background noise and/or streak artifacts.

In order to verify the statistical significance of the claimed improvement of image quality, the studies above were repeated by use of an ensemble of 500 noisy simulated sinograms. The noise

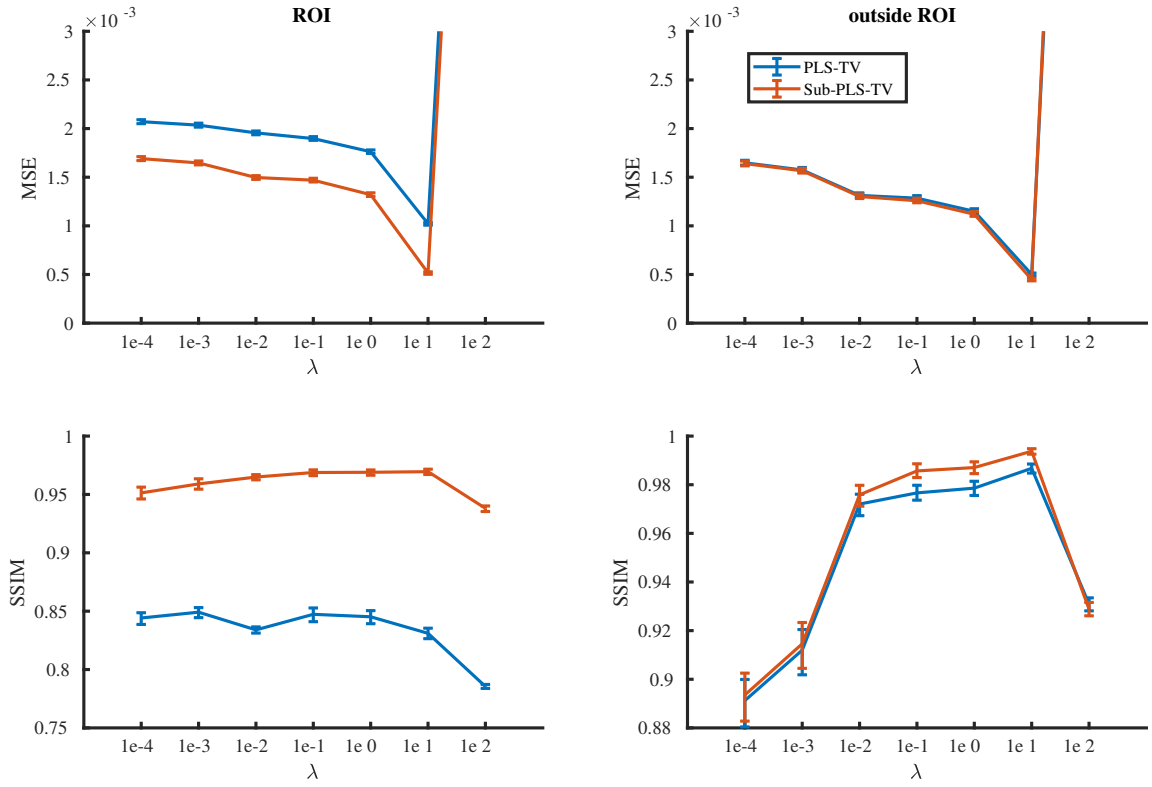

Fig 8 The mean MSE (top row) and SSIM (bottom row) values corresponding to images reconstructed by use of the PLS-TV (blue curve) and Sub-PLS-TV (red curve) methods as a function of regularization parameter value. Also shown are the 95% confidence intervals. The left and right columns correspond to the ROIs shown in Figs. 4 and 5, respectively.

model and level were the same as described above. From these data, ensembles of noisy reconstructed images were produced by use of the PLS-TV and Sub-PLS-TV methods corresponding to different regularization parameter values. From each ensemble of reconstructed images, the mean square error (MSE) and structure similarity index (SSIM) were computed in the two ROIs that were considered in Figs. 4 and 5. These values are plotted as a function of regularization parameter value in Fig. 8. The 95% confidence intervals are also displayed. The range of regularization parameter values is wider than that considered in Figs. 4 and 5 for the purpose of including the turning point of the curves. Note that when λ is large enough, both MSE and SSIM performances will eventually degrade. These results confirm that the improved performance of the Sub-PLS-TV

method is statistically significant.

5.2 Experimental studies

The proposed reconstruction method was also validated by use of an experimental D-XPCT data set produced by a benchtop edge-illumination X-ray phase contrast CT system built at University College London.[63,64] The sample was a dung beetle. The complete tomographic data set contained 720 views with an angular spacing of $0.5°$, from which a reference image could be generated via the FBP algorithm, which is shown in Fig 9. Detailed features of the object are visible in the zoomed-in region.

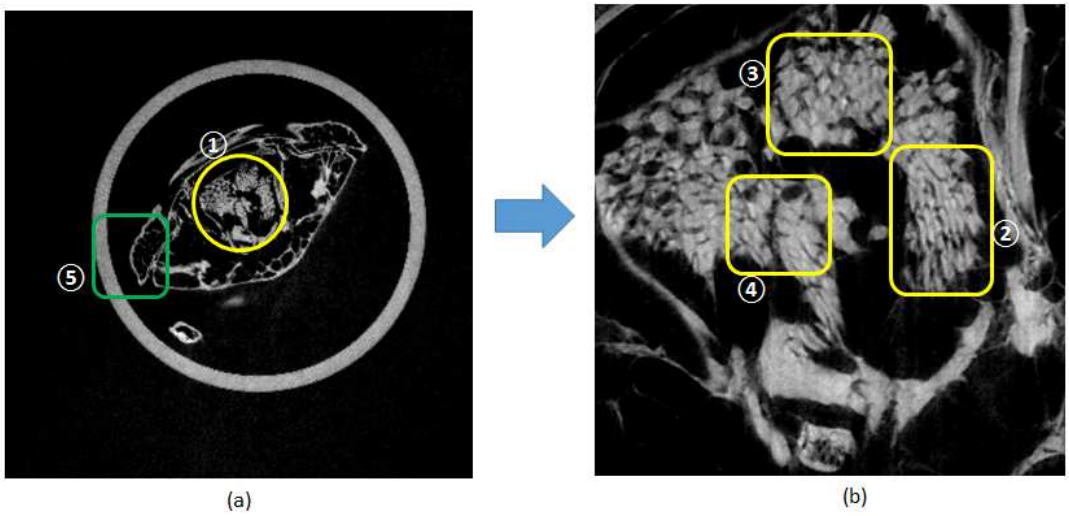

Fig 9 (a) The reference image of the object produced by use of the FBP algorithm and the complete data. (b) A zoomed-in region of the central part of the image correspoding to the designated ROI ①

For the few-view image reconstruction studies, a subset of 120 uniformly spaced views over a $180°$ span were extracted from the complete data set. This reduction in the number of measurements can reduce the acquisition times by one-sixth, resulting in a total time savings of an hour. Assuming the object's maximum frequency of interest is approximately 10 mm^{-1}, a central ROI with the radius of 2 mm (150 pixels) can be designated, where a reliable reconstruction of

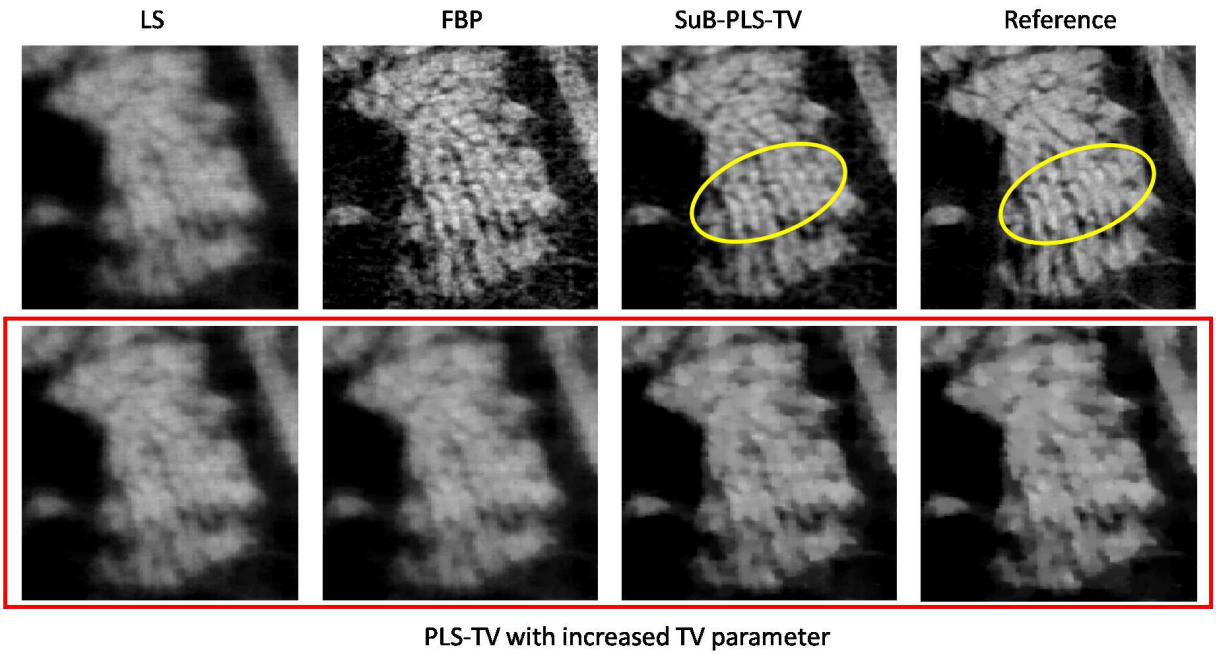

Fig 10 The comparison of the reconstructed ROI ② by use of FBP, PLS-TV and SuB-PLS-TV methods.

high-frequency structures is expected. The designated ROI is labeled as region ① in Fig 9. Three smaller windows ②-④ inside this ROI, as well as an outside-ROI region ⑤, will be inspected for evaluating the few-view reconstruction performances.

Figure 10 shows the reconstructed ROI images corresponding to the region ② labeled in Fig 9. The LS image indicates the least-square estimate of the object (i.e. Eq. (21) with $\lambda = 0$). It exhibits blurring appearance due to the nature of few-view data acquisition and the consequent insufficient sampling of high frequency contents in the Fourier domain. The image reconstructed by use of the FBP method preserves high-frequency details, but also contains a considerable amount of noise. In the bottom row, a series of images reconstructed by the PLS-TV method are shown with a wide range of increasing regularization parameter values that are listed in Table 1. As demonstrated before, they either appear blurred or oversmoothed. Instead, the proposed SuB-PLS-TV method provides promising results. The plotted ellipse highlights the structures that bear a close resemblance with the reference image while the conventional PLS-TV images do not have. In this study,

the choice of the regularization parameter value for the presented SuB-PLS-TV image is fixed the same as the one for the third PLS-TV image for all Figs. (10)-(13).

Similar observations resulted when examining the other two ROIs labeled as region ③ and ④. The reconstructed images and the comparison between different methods are shown in Figs 11 and 12. Again, all the images reconstructed by use of the PLS-TV method do not show the trend of resolving those fine structures, but the proposed SuB-PLS-TV method could produce a noise-suppressed and more natrual looking image that is very close to the reference.

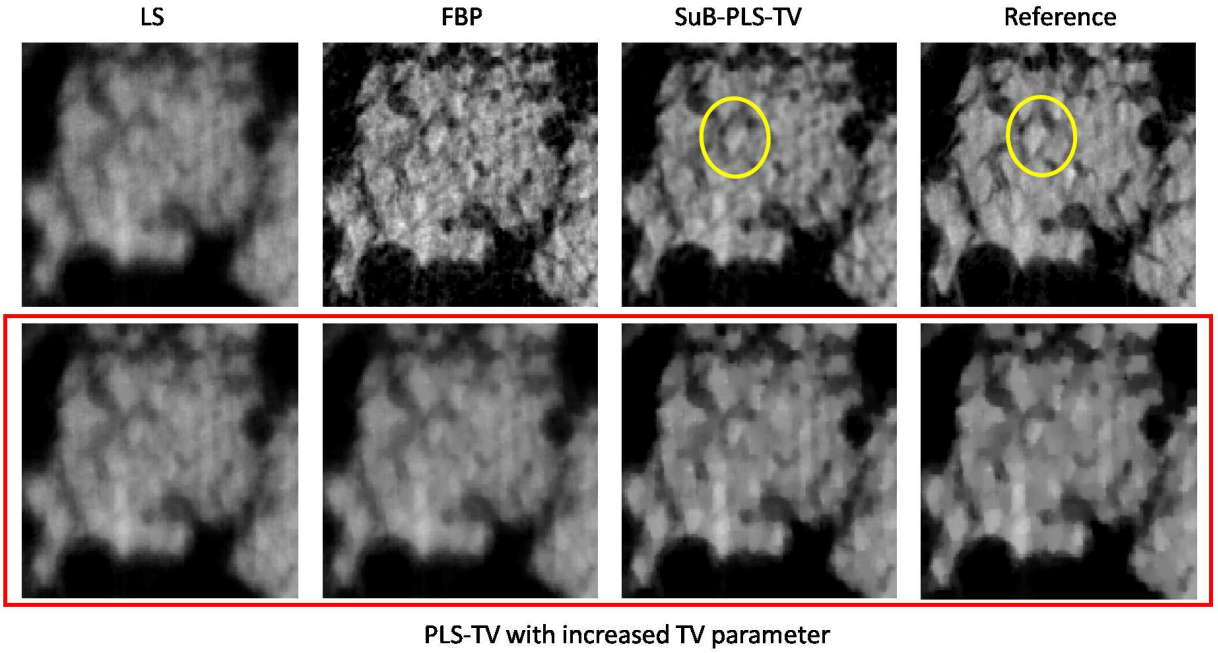

Fig 11 The comparison of the reconstructed ROI ③ by use of FBP, PLS-TV and SuB-PLS-TV methods.

Figure 13 shows a typical region ⑤ outside the designated central ROI ①. In this case, the SuB-LS-TV image gives a cleaner background compared with the FBP algorithm. It also visually outperforms the PLS-TV image in terms of restoring the structures located far from the center as indicated in the plotted ellipse.

All the images in Figs. (10)-(13) reconstructed by use of the PLS-TV, FBP and SuB-PLS-

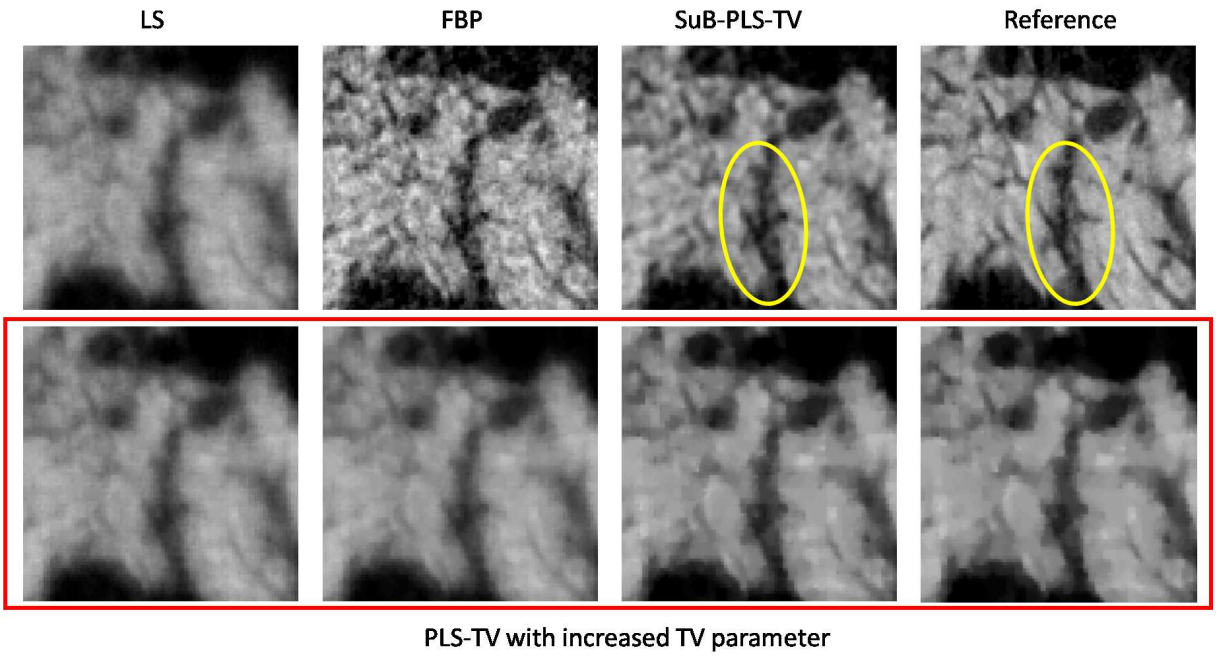

Fig 12 The comparison of the reconstructed ROI ④ by use of FBP, PLS-TV and SuB-PLS-TV methods.

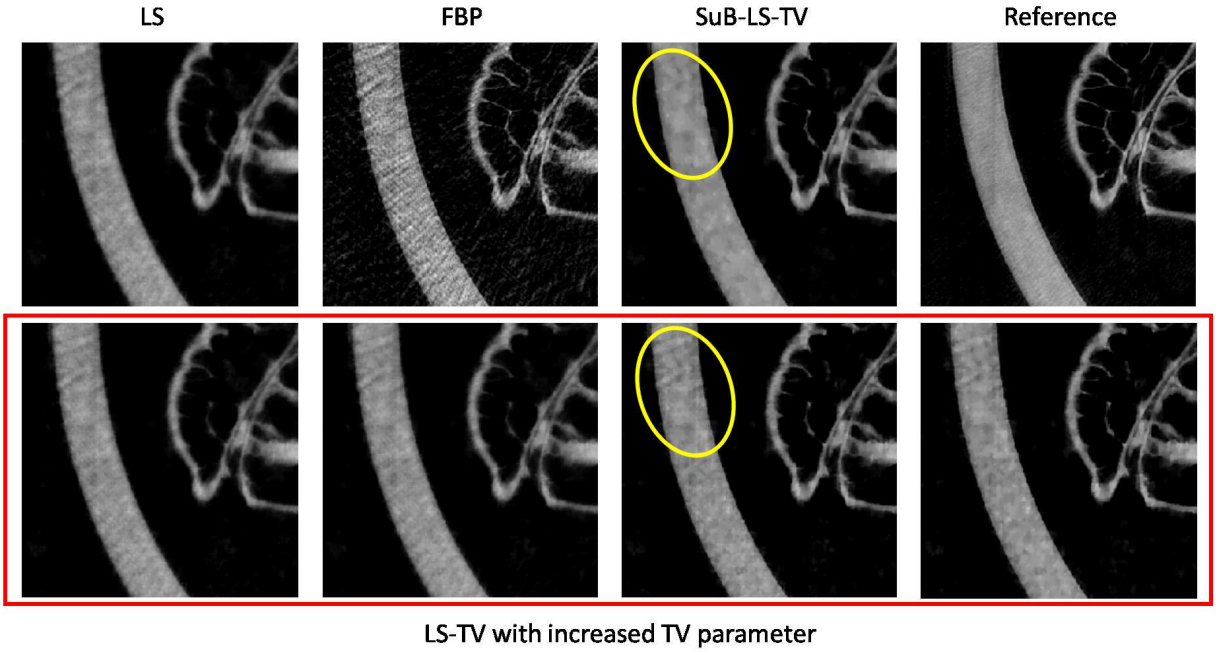

Fig 13 The comparison of the reconstructed region ⑤ outside the designated ROI by use of FBP, PLS-TV and SuB-PLS-TV methods.

TV methods were quantitatively evaluated in terms of Mean Square Error (MSE) and Structure Similarity Index (SSIM), as shown in Table 1. The images reconstructed from the complete dataset were served as the golden standard when computing all the figure of merits. In this study, a wide range of TV parameter values was scanned in order to reflect the overall trend of the performances for the conventional PLS-TV method. It can be observed that, in all listed regions, the SuB-PLS-TV method with an optimal TV parameter value ($\lambda = 3e^{-8}$) produced the lower MSE and higer SSIM values no matter what TV parameter value was chosen for the PLS-TV method. These results are consistent with the computer-simulation studies.

Table 1 Quantitative evaluation of the reconstructed images in MSE and SSIM

		PLS-TV w/ increasing TV parameter								FBP	SuB-PLS-TV
λ		$1e^{-8}$	$2e^{-8}$	$3e^{-8}$	$4e^{-8}$	$5e^{-8}$	$5e^{-7}$	$5e^{-6}$	$5e^{-5}$	-	$3e^{-8}$
②	MSE	5.030	4.972	5.029	4.991	4.901	4.433	4.307	6.351	4.771	4.292
	SSIM	0.667	0.671	0.675	0.675	0.681	0.712	0.717	0.615	0.683	0.754
③	MSE	5.296	5.229	4.975	4.924	4.799	4.272	4.207	5.914	4.529	4.185
	SSIM	0.685	0.690	0.708	0.706	0.714	0.746	0.746	0.674	0.768	0.777
④	MSE	5.082	5.021	4.880	4.818	4.739	4.318	4.242	6.627	4.728	4.209
	SSIM	0.681	0.687	0.700	0.699	0.705	0.729	0.729	0.632	0.728	0.774
⑤	MSE	4.401	4.212	4.110	4.085	4.079	3.731	3.731	5.917	5.480	3.625
	SSIM	0.560	0.579	0.588	0.589	0.589	0.612	0.614	0.526	0.450	0.623

6 Conclusion

A new subspace-based reconstruction strategy was proposed and investigated for use in few-view D-XPCT image reconstruction. It possesses the attractive feature that subtle structures can be accurately reconstructed within a designated ROI, while the entire FOV can be effectively regularized to mitigate noise and streaking artifacts. More specifically, the object is split into two components that represent the high-frequency and low-frequency subspaces, respectively. The resulting two-step iterative method is expected to mitigate the high-frequency information loss caused by data

incompleteness and produce better images than those produced by use of a conventional PLS-TV estimator. The proposed SuB-PLS-TV method was validated by a computer-simulated data set as well as an experimental data set acquired from an edge-illumination XPCT scanner.

The proposed reconstruction method can be applied with all XPCI imaging modalities that produce differential phase-contrast data. It can also be readily extended to conventional CT scenarios by use of a modified filter $C = \mathcal{R}\mathcal{R}^{\dagger}C_0$ in Eq. (12), where C_0 is the ramp filter in this case. In practical applications, the prior information regarding the maximum frequency of the sample may not be known, but Ω can be preset based on the maximum frequency of interest in terms of a specific imaging purpose. The projection data might need to be preprocessed with a low-pass filter according to the cut-off frequency Ω. Multiple trials for determining an ideal Ω may be necessary before the resulting image quality is fully optimized. Note that there is always a trade off between the frequency setting Ω and the size of the recoverable ROI.

It is worthy noting that the error term ϵ presented in Eq. (13) might affect the reconstructed images. When ϵ is not small, generally the reconstructed ROI is still sharp but the recovery of the high-frequency structures is at the cost of the appearance of streak artifacts. However, it should be noted that in the medical imaging field the task-based image assessment is widely promoted.[56] In some imaging applications, resolution-enhaced images are useful for diagnostic purposes even though the artifacts are sometimes present, and the proposed strategy is able to provide such a solution.

Appendix A: The derivation of the high-frequency subspace

Below we describe how Eq. (13) is derived, in which we claim $Wf_1 = Wf_{\text{null}} + \epsilon$, where f_1 is the solution of the optimization problem stated in Eq. (12), f_{null} is denoted as the null component of

the object with respect to the D-XPCT imaging operator $\mathcal{H} = \mathcal{D}\mathcal{R}$, and ϵ is the same error term as presented in Eq. (11).

Consider the optimization problem proposed in Eq. (12)

$$f_1 = \underset{f}{\operatorname{argmin}} \|f\|^2$$

$$s.t.\ \mathcal{H}f = (C-1)g.$$

By use of the pseudo-inverse of the imaging operator, denoted as $\mathcal{H}^{\#}$, the solution of the above optimization problem can be expressed analytically as

$$\begin{aligned} f_1 =& \mathcal{H}^{\#}(C-1)g \\ =& \mathcal{H}^{\#}Cg - \mathcal{H}^{\#}g. \end{aligned}$$

By use of the filter $C = \mathcal{H}\mathcal{R}^{\dagger}C_h$, as specified in Eq. (12), and the defined forward operator $\mathcal{H} = \mathcal{D}\mathcal{R}$, we can expand the above equation

$$\begin{aligned} f_1 =& H^{\#}\mathcal{H}\mathcal{R}^{\dagger}C_h g - \mathcal{H}^{\#}g \\ =& (\mathcal{D}\mathcal{R})^{\#}(\mathcal{D}\mathcal{R})\mathcal{R}^{\dagger}C_h g - \mathcal{H}^{\#}g \\ =& \mathcal{R}^{\#}\mathcal{D}^{\#}\mathcal{D}\mathcal{R}\mathcal{R}^{\dagger}C_h g - \mathcal{H}^{\#}g. \end{aligned}$$

In common situations where there is no truncation in the projection data, the derivative operator $\mathcal{D}$ is actually invertible with the properly defined boundary conditions. Therefore, $\mathcal{D}^{\#}\mathcal{D}$ can be cancelled such that

$$\begin{aligned} f_1 =& \mathcal{R}^{\#}\mathcal{R}\mathcal{R}^{\dagger}C_h g - \mathcal{H}^{\#}g \\ =& \mathcal{R}^{\dagger}C_h g - \mathcal{H}^{\#}g, \end{aligned}$$

in which the identity $\mathcal{R}^{\#}\mathcal{R}\mathcal{R}^{\dagger} = \mathcal{R}^{\dagger}$ is a property for linear operators.[56] Note that $\mathcal{R}^{\dagger}C_h g$ is exactly the FBP image as indicated in Eq. (4). This establishes that

$$f_1 = \hat{f}_{\text{FBP}} - \mathcal{H}^{\#} g.$$

By applying the mask W to f_1 and using the conclusion $W\hat{f}_{\text{FBP}} = Wf + \epsilon$ stated in Eq. (11),

$$\begin{aligned} Wf_1 =& W\hat{f}_{\text{FBP}} - W\mathcal{H}^{\#} g \\ =& Wf - W\mathcal{H}^{\#} g + \epsilon \\ =& W(f - \mathcal{H}^{\#} g) + \epsilon. \end{aligned}$$

Since the measurable component of the object f_{meas} is equivalent to $\mathcal{H}^{\#} g$,

$$\begin{aligned} Wf_1 =& W(f - f_{\text{meas}}) + \epsilon \\ =& Wf_{\text{null}} + \epsilon, \end{aligned}$$

which yields the conclusion in Eq. (13).

No conflicts of interest, financial or otherwise, are declared by the authors.

Acknowledgments

This work was supported in part by NIH awards EB02060401, EB02304501, NSF award CBET1263988, EPSRC grants EP/I021884/1 and EP/L001381/1.

References

1 F. Pfeiffer, C. Kottler, O. Bunk, *et al.*, "Hard x-ray phase tomography with low-brilliance sources," *Physical review letters* **98**(10), 108105 (2007).

2 T. Davis, D. Gao, T. Gureyev, *et al.*, "Phase-contrast imaging of weakly absorbing materials using hard x-rays," *Nature* **373**(6515), 595–598 (1995).

3 F. Pfeiffer, T. Weitkamp, O. Bunk, *et al.*, "Phase retrieval and differential phase-contrast imaging with low-brilliance x-ray sources," *Nature physics* **2**(4), 258–261 (2006).

4 R. Lewis, "Medical phase contrast x-ray imaging: current status and future prospects," *Physics in medicine and biology* **49**(16), 3573 (2004).

5 S. C. Mayo, A. W. Stevenson, and S. W. Wilkins, "In-line phase-contrast x-ray imaging and tomography for materials science," *Materials* **5**(5), 937–965 (2012).

6 A. A. Appel, J. C. Larson, A. B. Garson, *et al.*, "X-ray phase contrast imaging of calcified tissue and biomaterial structure in bioreactor engineered tissues," *Biotechnology and bioengineering* **112**(3), 612–620 (2015).

7 H. Guan, Q. Xu, A. B. Garson III, *et al.*, "Boundary-enhancement in propagation-based x-ray phase-contrast tomosynthesis improves depth position characterization," *Physics in medicine and biology* **60**(8), N151 (2015).

8 A. Bravin, P. Coan, and P. Suortti, "X-ray phase-contrast imaging: from pre-clinical applications towards clinics," *Physics in medicine and biology* **58**(1), R1 (2012).

9 X. Wu and H. Liu, "Clinical implementation of x-ray phase-contrast imaging: Theoretical foundations and design considerations," *Medical physics* **30**(8), 2169–2179 (2003).

10 T. Gureyev, S. Mayo, D. Myers, *et al.*, "Refracting röntgens rays: propagation-based x-ray phase contrast for biomedical imaging," *Journal of Applied Physics* **105**(10), 102005 (2009).

11 D. Chapman, W. Thomlinson, R. Johnston, *et al.*, "Diffraction enhanced x-ray imaging," *Physics in medicine and biology* **42**(11), 2015 (1997).

12 M. N. Wernick, O. Wirjadi, D. Chapman, *et al.*, "Multiple-image radiography," *Physics in medicine and biology* **48**(23), 3875 (2003).

13 L. Rigon, H.-J. Besch, F. Arfelli, *et al.*, "A new dei algorithm capable of investigating sub-pixel structures," *Journal of Physics D: Applied Physics* **36**(10A), A107 (2003).

14 F. Noo, R. Clackdoyle, and J. D. Pack, "A two-step hilbert transform method for 2d image reconstruction," *Physics in Medicine & Biology* **49**(17), 3903 (2004).

15 T. Weitkamp, A. Diaz, C. David, *et al.*, "X-ray phase imaging with a grating interferometer," *Optics express* **13**(16), 6296–6304 (2005).

16 C. Hagen, P. Munro, M. Endrizzi, *et al.*, "Low-dose phase contrast tomography with conventional x-ray sources," *Medical physics* **41**(7) (2014).

17 C. Hagen, P. Diemoz, M. Endrizzi, *et al.*, "Theory and preliminary experimental verification of quantitative edge illumination x-ray phase contrast tomography," *Optics express* **22**(7), 7989–8000 (2014).

18 Y. Chen, H. Guan, C. K. Hagen, *et al.*, "Single-shot edge illumination x-ray phase-contrast tomography enabled by joint image reconstruction," *Optics Letters* **42**(3), 619–622 (2017).

19 M. Endrizzi, F. Vittoria, L. Rigon, *et al.*, "X-ray phase-contrast radiography and tomography with a multiaperture analyzer," *Physical Review Letters* **118**(24), 243902 (2017).

20 C.-Y. Chou, M. A. Anastasio, J. G. Brankov, *et al.*, "An extended diffraction-enhanced imaging method for implementing multiple-image radiography," *Physics in medicine and biology* **52**(7), 1923 (2007).

21 M. Nilchian, Z. Wang, T. Thuering, *et al.*, "Spline based iterative phase retrieval algorithm for x-ray differential phase contrast radiography," *Optics express* **23**(8), 10631–10642 (2015).

22 P. Diemoz, M. Endrizzi, C. Hagen, *et al.*, "Edge illumination x-ray phase-contrast imaging: nanoradian sensitivity at synchrotrons and translation to conventional sources," in *Journal of Physics: Conference Series*, **499**(1), 012006, IOP Publishing (2014).

23 D. Snyder and J. Cox, "An overview of reconstructive tomography and limitations imposed by a finite number of projections," *Reconstruction Tomography in Diagnostic Radiology and Nuclear Medicine* , 28 (1977).

24 G. W. Faris and R. L. Byer, "Three-dimensional beam-deflection optical tomography of a supersonic jet," *Applied Optics* **27**(24), 5202–5212 (1988).

25 Z.-F. Huang, K.-J. Kang, L. Zhang, *et al.*, "Alternative method for differential phase-contrast imaging with weakly coherent hard x rays," *Physical Review A* **79**(1), 013815 (2009).

26 E. Y. Sidky, C.-M. Kao, and X. Pan, "Accurate image reconstruction from few-views and limited-angle data in divergent-beam ct," *Journal of X-ray Science and Technology* **14**(2), 119–139 (2006).

27 J. Bian, J. H. Siewerdsen, X. Han, *et al.*, "Evaluation of sparse-view reconstruction from flat-panel-detector cone-beam ct," *Physics in medicine and biology* **55**(22), 6575 (2010).

28 Y. Zhang, W.-H. Zhang, H. Chen, *et al.*, "Few-view image reconstruction combining total

variation and a high-order norm," *International Journal of Imaging Systems and Technology* **23**(3), 249–255 (2013).

29 G. L. Zeng, "On few-view tomography and staircase artifacts," *Nuclear Science, IEEE Transactions on* **62**(3), 851–858 (2015).

30 E. Y. Sidky, C.-M. Kao, and X. Pan, "Effect of the data constraint on few-view, fan-beam ct image reconstruction by tv minimization," in *Nuclear Science Symposium Conference Record, 2006. IEEE*, **4**, 2296–2298, IEEE (2006).

31 H. Yu and G. Wang, "A soft-threshold filtering approach for reconstruction from a limited number of projections," *Physics in medicine and biology* **55**(13), 3905 (2010).

32 Q. Xu, E. Y. Sidky, X. Pan, *et al.*, "Investigation of discrete imaging models and iterative image reconstruction in differential x-ray phase-contrast tomography," *Optics express* **20**(10), 10724–10749 (2012).

33 T. Köhler, B. Brendel, and E. Roessl, "Iterative reconstruction for differential phase contrast imaging using spherically symmetric basis functions," *Medical physics* **38**(8), 4542–4545 (2011).

34 M. Nilchian, C. Vonesch, P. Modregger, *et al.*, "Fast iterative reconstruction of differential phase contrast x-ray tomograms," *Optics express* **21**(5), 5511–5528 (2013).

35 M. Nilchian, C. Vonesch, S. Lefkimmiatis, *et al.*, "Constrained regularized reconstruction of x-ray-dpci tomograms with weighted-norm," *Optics express* **21**(26), 32340–32348 (2013).

36 E. J. Candès and M. B. Wakin, "An introduction to compressive sampling," *IEEE Signal Processing Magazine* **25**(2), 21–30 (2008).

37 Q. Xu, A. Sawatzky, M. A. Anastasio, *et al.*, "Sparsity-regularized image reconstruction of decomposed k-edge data in spectral ct," *Physics in medicine and biology* **59**(10), N65 (2014).

38 J.-L. Starck, F. Murtagh, and J. M. Fadili, *Sparse image and signal processing: wavelets, curvelets, morphological diversity*, Cambridge university press (2010).

39 Q. Xu, H. Yu, X. Mou, *et al.*, "Low-dose x-ray ct reconstruction via dictionary learning," *IEEE Transactions on Medical Imaging* **31**(9), 1682–1697 (2012).

40 S. Ravishankar and Y. Bresler, "Mr image reconstruction from highly undersampled k-space data by dictionary learning," *IEEE transactions on medical imaging* **30**(5), 1028–1041 (2011).

41 Z. Zhu, K. Wahid, P. Babyn, *et al.*, "Improved compressed sensing-based algorithm for sparse-view ct image reconstruction," *Computational and mathematical methods in medicine* **2013** (2013).

42 Z. Tian, X. Jia, K. Yuan, *et al.*, "Low-dose ct reconstruction via edge-preserving total variation regularization," *Physics in medicine and biology* **56**(18), 5949 (2011).

43 C. Kottler, F. Pfeiffer, O. Bunk, *et al.*, "Grating interferometer based scanning setup for hard x-ray phase contrast imaging," *Review of Scientific Instruments* **78**(4), 043710 (2007).

44 P. R. Munro, K. Ignatyev, R. D. Speller, *et al.*, "Phase and absorption retrieval using incoherent x-ray sources," *Proceedings of the National Academy of Sciences* **109**(35), 13922–13927 (2012).

45 P. R. Munro, C. K. Hagen, M. B. Szafraniec, *et al.*, "A simplified approach to quantitative coded aperture x-ray phase imaging," *Optics express* **21**(9), 11187–11201 (2013).

46 K.-H. Yoon, J. H. Ryu, C. W. Jung, *et al.*, "Differential x-ray phase-contrast imaging with a grating interferometer using a laboratory x-ray micro-focus tube," *Journal of the Korean Physical Society* **65**(12), 2111–2116 (2014).

47 J. Fu, R. Tan, and L. Chen, "Analysis and accurate reconstruction of incomplete data in x-ray differential phase-contrast computed tomography," *Analytical and bioanalytical chemistry* **406**(3), 897–904 (2014).

48 B. Logan *et al.*, "The uncertainty principle in reconstructing functions from projections," *Duke Math. J* **42**(4), 661–706 (1975).

49 A. K. Louis, "Orthogonal function series expansions and the null space of the radon transform," *SIAM journal on mathematical analysis* **15**(3), 621–633 (1984).

50 A. Caponnetto and M. Bertero, "Tomography with a finite set of projections: singular value decomposition and resolution," *Inverse problems* **13**(5), 1191 (1997).

51 A. K. Louis, "Nonuniqueness in inverse radon problems: the frequency distribution of the ghosts," *Mathematische Zeitschrift* **185**(3), 429–440 (1984).

52 P. M. Joseph and R. A. Schulz, "View sampling requirements in fan beam computed tomography," *Medical physics* **7**(6), 692–702 (1980).

53 A. Rieder and A. Faridani, "The semidiscrete filtered backprojection algorithm is optimal for tomographic inversion," *SIAM journal on numerical analysis* **41**(3), 869–892 (2003).

54 X. Pan, "Quasi-bandlimited properties of radon transforms and their implications for increasing angular sampling densities," *IEEE transactions on medical imaging* **17**(3), 395–406 (1998).

55 G. L. Zeng, "Comparison of fbp and iterative algorithms with non-uniform angular sampling," *Nuclear Science, IEEE Transactions on* **62**(1), 120–130 (2015).

56 H. H. Barrett and K. J. Myers, *Foundations of image science*, John Wiley & Sons (2013).

57 T. Nikazad, *The use of Landweber algorithm in image reconstruction*. PhD thesis, Matematiska institutionen (2007).

58 R. M. Lewitt, "Multidimensional digital image representations using generalized kaiser–bessel window functions," *JOSA A* **7**(10), 1834–1846 (1990).

59 S. Matej and R. M. Lewitt, "Practical considerations for 3-d image reconstruction using spherically symmetric volume elements," *IEEE transactions on medical imaging* **15**(1), 68–78 (1996).

60 S. Matej and R. M. Lewitt, "Image representation and tomographic reconstruction using spherically-symmetric volume elements," in *Nuclear Science Symposium and Medical Imaging Conference, 1992., Conference Record of the 1992 IEEE*, 1191–1193, IEEE (1992).

61 A. Beck and M. Teboulle, "A fast iterative shrinkage-thresholding algorithm for linear inverse problems," *SIAM journal on imaging sciences* **2**(1), 183–202 (2009).

62 F. Bochud, C. Abbey, and M. Eckstein, "Statistical texture synthesis of mammographic images with super-blob lumpy backgrounds," *Optics express* **4**(1), 33–42 (1999).

63 A. Olivo and R. Speller, "A coded-aperture technique allowing x-ray phase contrast imaging with conventional sources," *Applied Physics Letters* **91**(7), 074106 (2007).

64 C. K. Hagen, P. C. Diemoz, M. Endrizzi, *et al.*, "Quantitative edge illumination x-ray phase contrast tomography," in *SPIE Optical Engineering+ Applications*, 921205–921205, International Society for Optics and Photonics (2014).